Available online at www.sciencedirect.com
SCIENCE DIRECT®
Pergamon
Acta Materialia 51 (2003) 1421–1436
Acta MATERIALIA
www.actamat-journals.com

Nano-structures at martensite macrotwin interfaces in $Ni_{65}Al_{35}$

Ph. Boullay [a,1], D. Schryvers [a,*], J.M. Ball [b]

[a] *EMAT, University of Antwerp, RUCA, Groenenborgerlaan 171, B-2020 Antwerpen, Belgium*
[b] *Mathematical Institute, University of Oxford, 24-29 St Giles, Oxford OX1 3LB, UK*

Received 8 July 2002; received in revised form 2 October 2002; accepted 29 October 2002

Abstract

The atomic configurations at macrotwin interfaces between microtwinned martensite plates in $Ni_{65}Al_{35}$ material are investigated using transmission electron microscopy. The observed structures are interpreted in view of possible formation mechanisms for these interfaces. A distinction is made between cases in which the microtwins, originating from mutually perpendicular {110} austenite planes, enclose a final angle larger or smaller than 90°. Two different configurations, a crossing and a step type are described. Depending on the actual case, tapering, bending and tip splitting of the smaller microtwin variants are observed. The most reproducible deformations occur in a region of approximately 5–10 nm width around the interface while a variety of structural defects are observed further away from the interface. These structures and deformations are interpreted in terms of the coalescence of two separately nucleated microtwinned martensite plates and the need to accommodate remaining stresses.

Keywords: Martensite; Twinning; Electron microscopy; Nonlinear thermoelasticity

1. Introduction

In this paper we describe experimental observations using conventional and high resolution transmission electron microscopy ((HR)TEM) of macrotwin interfaces between microtwinned martensitic plates in bulk and splat-cooled $Ni_{65}Al_{35}$, and we attempt to understand how some of the observed features arise in terms of the deformation process starting from the cubic austenite.

A fundamental problem for martensitic transformations is to predict the morphology of the microstructure arising in a given experimental situation. This is a challenging problem of pattern formation, but one that is currently out of reach because of the major difficulties of modelling, analysis and computation that it gives rise to. Considerable insight has, however, been gained by the use of static continuum theories based on elasticity and variants of it (e.g., incorporating interfacial energy). Under idealized assumptions about the crystal, for example that it is a single crystal free

* Corresponding author. Tel.: +32-3-2180-247; fax: +32-3-2180-257.
E-mail address: nick.schryvers@ua.ac.be (D. Schryvers).
[1] Now at Laboratoire SPCTS, Faculté des Sciences, 123 Av. Albert Thomas, 87060 Limoges Cedex, France.

1359-6454/03/$30.00 © 2003 Acta Materialia Inc. Published by Elsevier Science Ltd. All rights reserved.
doi:10.1016/S1359-6454(02)00536-0

of defects, and about its thermo-mechanical environment, such theories provide significant information on possible microstructures, and in particular illuminate the role of geometric compatibility. However, they are not truly predictive in the sense that typically they permit many different equi-energetic configurations. (Of course, it might be that a good dynamical model might have unstable or chaotic properties that make it non-predictive also, but that is a different issue.) Also, in reality the idealized assumptions made are often questionable. For example, only very high quality bulk single crystals will have relatively few defects. Most samples exist as regular ingots, for which the implications of the static theories are less precise, and inside the sample the local microstructure will depend on such features as the relative orientation between grains, the different grain sizes, slight composition differences and thus different transformation temperatures, different temperature histories due to different locations within the ingot etc. Such differences can even be enhanced by using special preparation techniques such as melt-spinning or splat-cooling. Moreover, the effects arising from the dynamic nature of a first-order transformation involving several progressing interfaces add many more degrees of freedom than those considered in the static models.

In the present work atomic details of particular microscopic configurations resulting from the cubic-to-tetragonal martensitic transformation in $Ni_{65}Al_{35}$ will be discussed. At this composition, the transformation occurs at around 250 °C [1]. The ideal orientation relationships between, e.g., twin and habit planes have been predicted before by the conventional crystallographic theories and have in some cases already been documented for this transformation [2–4]. However, the actual atomic configurations at the interfaces reveal remarkable features which indicate a higher level of complexity than current theoretical discussions take into account. In this paper, the emphasis of the experimental data will be on macrotwin interfaces involving two families of microtwin planes and two out of the three possible deformation variants of the martensite. This choice implies that the microtwins in the two plates involved originate from two perpendicular {110} families of planes in the austenite.

Unfortunately, the high speed and small hysteresis of the transformation usually result in completely transformed samples at room temperature and major difficulties for in-situ temperature work, the latter also being hampered by thin foil effects in transmission electron microscopy samples. As a result, the actual dynamic origin of a given structure usually cannot be followed directly and has to be inferred from its final configuration. In this paper details of such configurations are described based on room temperature (HR)TEM observations. These configurations are then discussed in terms of the dynamics of the austenite–martensite transformation, which play an essential role in the shape–memory behaviour of many of these alloys.

2. Experimental procedures

Ni–Al bulk material with a Ni content of 65 at % Ni was prepared in the form of ingots by arc melting starting from 99.99% pure elements. The ingots were homogenised by annealing for 1 h at 1250 °C, followed by a water quench. Alternatively, Ni–Al splat-cooled samples of the same composition were prepared by pressing a free falling droplet of the melt in between two copper pistons that were shot against each other with a velocity of 8 $m.s^{-1}$. The solidification of the melt results from the heat transfer occurring during the contact of the pistons with the melt. A cooling rate of approximately 9×10^5 $K.s^{-1}$ is obtained. The resulting discs have a diameter of approximately 20 mm and a thickness of about 200 μm. From both bulk and splat-cooled samples, 3 mm diameter discs suitable for TEM observations were obtained. These discs were then thinned by the double-jet electropolishing technique using a Struers Tenupol-3 instrument [5]. Whenever relevant, the origin of every image shown is indicated, although no firm distinctions between the results from bulk versus splat-cooled samples could be drawn.

Electron diffraction work and low magnification observations were carried out using a Philips CM20 microscope operating at 200 kV and fitted

with an eucentric goniometer (±45°). The HRTEM images were recorded on a JEOL 4000EX top-entry microscope (double-tilt ±20°) operating at 400 kV. Both instruments are equipped with a LaB_6 filament.

3. The martensitic transformation in Ni–Al

In order to be able to describe the observations properly, we first give a short description of the transformation and the structures involved. For clarity we will also briefly recall the description of the martensitic transformation in the framework of nonlinear thermoelasticity [6–8], a more rigorous and general approach than the classical crystallographic theories [9–12], with a focus on the cubic-to-tetragonal transition encountered in the Ni–Al alloys [13,14].

In the nonlinear thermoelasticity approach, microstructural features such as twins in martensite or austenite/martensite interfaces are described by minimizers and minimizing sequences for the bulk elastic energy corresponding to a free energy density $\phi(\mathbf{F}, \theta)$ which depends only on the deformation gradient $\mathbf{F} = \nabla y(x)$ and the temperature θ. A first fundamental invariance property of the free energy function is its frame-indifference, i.e. invariance under rigid body rotations, namely that $\phi(\mathbf{RF}, \theta) = \phi(\mathbf{F}, \theta)$ for any rotation matrix $\mathbf{R}$. In particular, for any matrices $\mathbf{F}$ that minimize $\phi(\mathbf{F}, \theta)$, all matrices $\mathbf{RF}$ are also minimizers. The second invariance property results from the existence of symmetries within the crystal, namely $\phi(\mathbf{FQ}, \theta) = \phi(\mathbf{F}, \theta)$ for any $\mathbf{Q}$ in the point group.

The reference configuration is chosen to be the undistorted austenite at the austenite–martensite transformation temperature θ_0, and it is assumed that $\mathbf{F} = 1$ minimizes $\phi(\mathbf{F}, \theta_0)$. Due to frame indifference, all rotations $\mathbf{R}$ minimize $\phi(\mathbf{F}, \theta_0)$ and define what is called the austenite energy well.

During the transformation, the cubic lattice of the austenite is distorted to a tetragonal unit cell by elongating one of the cubic axes by a factor $\eta_3 > 1$ and shortening the other two by a factor $\eta_1 < 1$ (Figs. 1 and 2). In the homogeneous deformation $y = \mathbf{U}_1 x$, which transforms the austenite to the martensite, the matrix $\mathbf{U}_1$ represents the transformation strain or Bain strain and has the form $\mathbf{U}_1 = \mathrm{Diag}[\eta_3, \eta_1, \eta_1]$. We can regard $\mathbf{U}_1$ as the representation of one deformation variant of the martensite and it is assumed that $\mathbf{F} = \mathbf{U}_1$ minimizes $\phi(\mathbf{F}, \theta_0)$.

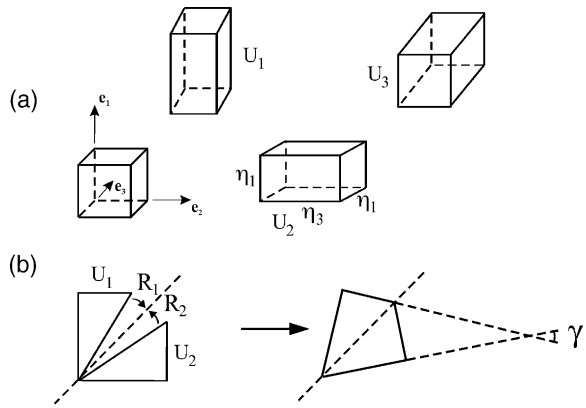

Fig. 1. (a) Schematic representation of the three equivalent deformation variants U_1, U_2 and U_3 existing when cubic austenite transforms into tetragonal martensite. (b) Schematic illustration of the need for rotations R_i in order to combine two different deformation variants into one martensite plate, including the definition of the angle γ.

Following symmetry considerations, the cubic-to-tetragonal transformation leads to the existence of three variants of martensite. The remaining two possibilities, $\mathbf{U}_2$ and $\mathbf{U}_3$, are obtained by permuting the diagonal elements of the matrix, so that $\mathbf{U}_2 = \mathrm{Diag}[\eta_1, \eta_3, \eta_1]$ and $\mathbf{U}_3 = \mathrm{Diag}[\eta_1, \eta_1, \eta_3]$. Using frame indifference, all matrices $\mathbf{F} = \mathbf{R}_i\mathbf{U}_i$ where $\mathbf{R}_i$ is a rotation, also minimize $\phi(\mathbf{F}, \theta_0)$ and define the ith martensite energy. In practice, these rotations are needed to close the gap between the lattices of both variants resulting from the deformation, as indicated in Fig. 1b. As a result, certain former parallel cubic planes and directions now enclose an angle γ as indicated in the figure. After the transformation the entire product microstructure should correspond to a continuous energy-minimizing deformation. For low energy microstructures the deformation gradient $\nabla y(x)$ must be close to the martensite energy wells in most of the sample. The requirement of continuity (for example, coherency at the austenite–martensite habit plane), the surface energy of the

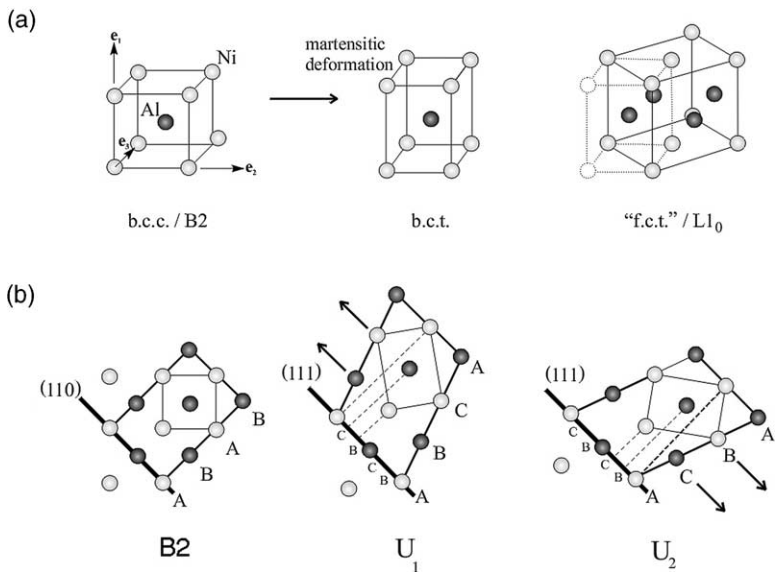

Fig. 2. (a) Schematic representation of the ordering in Ni–Al austenite and martensite, the latter with two possible choices for the unit cell (see also text). (b) Two-dimensional projection illustrating the formation of close packed ABC (or ACB) stackings and rectangular symmetry of the projected martensite lattice. The relative directions of shearing with respect to the (110) basal plane in the B2 austenite are indicated by arrows.

intervariant boundaries etc. play key roles in determining the possible final microstructures.

In the case of Ni–Al, the austenite phase has a CsCl-type ordering based on a body-centred-cubic (bcc) lattice and is often referred to as the β- or B2-phase (Fig. 2). The excess Ni is accommodated by random occupation of Ni atoms at the Al sublattice sites [15]. As the martensitic transformation is purely displacive, this ordering is retained in the martensite, as illustrated in Fig. 2a. Following conventional Bravais lattice notations, the martensite should be viewed as a body-centred-tetragonal (bct) lattice, but in order to account for the resulting $L1_0$ type (CuAu I) ordering in the martensite, this structure is traditionally described using a face-centred-tetragonal (fct) lattice and often referred to as the θ-phase. As a result, the microtwin planes of the product structure, which correspond to the invariant shear of the transformation, are {111} type planes in the $L1_0$ martensite structure and originate from certain {110} type planes of the austenite structure. As seen from Fig. 2a, the cubic axis that is elongated during the transformation always becomes the *c*-axis of the product fct cell. In the following discussion, the fct unit cell will be used for the description of the martensite lattice, although the bct cell corresponds with the tetragonal shapes of the three variants in Fig. 1.

When referring to this $L1_0$ structure the notion of close packed planes becomes relevant. Indeed, the cubic-to-tetragonal transformation deforms the open rectangular $\{110\}_{B2}$ planes into nearly hexagonal {111} planes of the face centred cell, which for the current ordering are as dense as possible. The first drawing of Fig. 2b shows a two-dimensional projection along a $<001>$ axis of the austenite structure, its cubic unit cell being indicated by faint lines. The other two drawings of Fig. 2b show the effect of transformations $\mathbf{U}_1$ and $\mathbf{U}_2$ (i.e., those with the elongation direction in the plane of the drawing) in this projection. When the original $(110)_{B2}$ plane indicated by a heavy line is used as a reference, these two variants yield different stacking sequences ABC and ACB of the close packed planes in the product structure. This is seen from the indicated projections (dashed lines) onto the, now $(111)_{L10}$, reference plane and which arrive at the fixed positions labeled A, B and C. The direction of projection is not exactly perpen-

dicular to the reference plane due to the fact that the $L1_0$ structure is not perfectly cubic but has a c/a ratio slightly deviating from unity. As the opposite stacking sequences for both variants can be regarded as resulting from opposite shearing directions (indicated by arrows in Fig. 2b), different volume fractions for variants $\mathbf{U}_1$ and $\mathbf{U}_2$ will yield a net total shearing for a given plate.

4. Relations between martensite variants and plates: conceptual discussion

In order to facilitate the interpretation of the experimental observations, we give in this section a conceptual discussion essentially based on energy minimization and with the emphasis on which type of interfaces can be expected. In the case of the first-order cubic-to-tetragonal transformation in Ni–Al, different martensite plates consisting of a sequence of two different variants of the product phase as defined above can nucleate and grow in the austenite matrix, as shown schematically in Fig. 3. Here the austenite is viewed along the $[001]_{B2}$ direction, which will also be the assumed viewing direction in the calculations discussed below, and the martensite along $<110]_{L10}$ directions, the latter depending on the actual variant. Within each plate both variants are in compound twin relation with one another and the resulting interfaces will henceforth be referred to as microtwin boundaries or simply microtwins. Minimization of the elastic energy yields unequal relative widths for both variants (except for special values of the deformation parameters [6,12,13]) resulting in a given volume fraction λ, a small rotation θ of the microtwin plane with respect to the corresponding $\{110\}_{B2}$ plane and a habit plane, i.e., the interface between the austenite and martensite regions, with normal **m**. For the present case this habit plane is close to a $\{101)_{B2}$ plane. Such planes make an angle of 60° with the $\{110)_{B2}$ planes, i.e., the planes in the parent phase that will transform into the microtwin planes for the present product variants. In fact, the angle ψ between the $\{110)_{B2}$ planes and the corresponding habit plane is given by the formula

$$\sin\psi = \sqrt{\frac{\eta_3^2-\eta_1^2}{2\eta_1^2(\eta_3^2-1)}}$$

which for the present deformation parameters (see Section 6) yields $\psi = 64.9°$.

As the final microtwin configuration depends on the deformation parameters, some measures such as the angle γ and the volume fraction λ of the smallest variant, can be calculated in terms of the deformation parameters:

$$\cos\gamma = \frac{2\eta_1\eta_3}{\eta_1^2 + \eta_3^2} \quad \text{and}$$

$$\lambda = \frac{1}{2}\left(1-\sqrt{1 + \frac{2(\eta_1^2-1)(\eta_3^2-1)(\eta_1^2 + \eta_3^2)}{(\eta_3^2-\eta_1^2)^2}}\right)$$

To a first approximation, both variants within a given plate rotate through equal and opposite angles $\pm\gamma/2$ about the normal to the plane of the drawing, forming microtwin planes parallel to the prior austenite (110) planes. However, compatibility with the austenite requires that there is a small rigid-body rotation of the entire plate that destroys this balance, so that the final orientation of one variant will be closer to its non-rotated tetragonal orientation than for the other, the microtwin planes not being exactly parallel with the prior austenite (110) planes.

As a result of the growth of such martensite plates, the entire austenite matrix is transformed, resulting in different interplate interfaces with atomic configurations depending on the actual variants and orientations in each of the impinging plates. If we disregard the local variations which indifferently occur in each plate (e.g., local deviations from the average volume fraction), those interfaces existing between prior plates with different families of microtwin planes (e.g., prior $(110)_{B2}$ and $(1\text{–}10)_{B2}$) but the same choice of variants (e.g., $\mathbf{U}_1$ and $\mathbf{U}_2$) can be considered as mirror planes and thus be called macrotwin boundaries or interfaces. When two such plates with close to perpendicular microtwins meet, it can be expected that this symmetry plane will be parallel to a cubic $\{100\}_{B2}$ plane, mirroring, e.g., $(110)_{B2}$ into $(1\text{–}10)_{B2}$ microtwins. Still, as different internal configurations for each plate can exist and as the kinetics

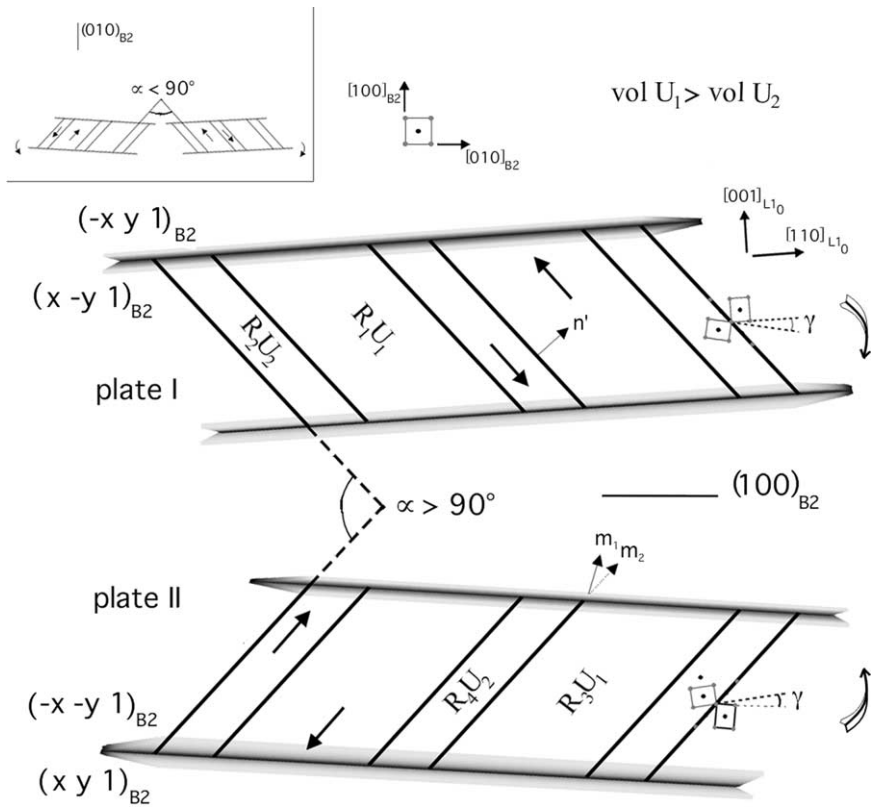

Fig. 3. Schematic representation of the relative orientations of different features of two martensite plates which will finally make contact along cubic B2 planes.

of the plate growth can also be expected to play a role, the exact choice of a $(100)_{B2}$ versus a $(010)_{B2}$ macrotwin plane can be more complicated.

For plate I in Fig. 3 the microtwin planes are chosen to originate from $(110)_{B2}$ planes and deformation variants $\mathbf{U}_1$ and $\mathbf{U}_2$ are combined, with $\mathbf{U}_1$ occupying the largest volume. These choices fix the exact orientation of the microtwin planes and limit the possibilities for the habit plane to two equivalent ones $(-x, y, 1)_{B2}$ and $(x, -y, 1)_{B2}$. In the figure, the microtwin planes are observed edge-on while the habit planes are inclined. Plate II uses the same deformation variants with the same volume ratio (i.e., again volume $\mathbf{U}_1$>volume $\mathbf{U}_2$), but a different set of microtwin planes, here $(1–10)_{B2}$, perpendicular to the previous family. Therefore crystallographically equivalent, but intrinsically different, habit planes will occur, again with two possible orientations. For the present introductory description any additional effects due to the small rigid body rotations are ignored. Suppose now that both plates nucleate separately in a given austenite grain. They can then join in different ways along a $\{100\}_{B2}$ plane. First, the choice of $\mathbf{U}_1$ as the variant with the largest volume fraction immediately implies different atomic configurations depending on the actual choice between a $(100)_{B2}$ or $(010)_{B2}$ plane as macrotwin. Indeed, joining along the $(100)_{B2}$ plane implies that the elongation directions (i.e., the fct *c*-axes) of variants $\mathbf{U}_1$ on either side are close to perpendicular to this new interface. On the other hand, joining along the $(010)_{B2}$ plane means that these directions are close to parallel with the formed macrotwin. These are features which can be recognized from the HRTEM images and will thus be helpful in characterising the macrotwin interfaces. Second, for each of the possibilities just listed, still two different habit planes

for each plate can be involved. The general expression for the two possible habit plane normals $\mathbf{m}_{1,2}$ per plate (one for each choice of χ) is given by

$$m_{1,2} = \left[\frac{\chi}{2}(\delta + \tau), \frac{\chi}{2}\kappa(\tau-\delta), 1\right] \quad \text{with}$$

$$\chi = \pm 1 \text{ where } \quad \delta = \sqrt{\frac{\eta_3^2 + \eta_1^2 - 2}{1-\eta_1^2}} \quad \text{and}$$

$$\tau = \sqrt{\frac{2\eta_1^2\eta_3^2 - \eta_3^2 - \eta_1^2}{1-\eta_1^2}}$$

where $\kappa = \pm 1$ defines the choice of microtwin plane orientation (i.e., $\kappa = +1$ yields plate I, $\kappa = -1$ yields plate II). Such habit planes are thus distinctly different from any symmetry plane of the austenite. As the Miller indices for the normals to these habit planes only differ in sign for the x and y co-ordinates, if the final joining plane is $(100)_{B2}$ or $(010)_{B2}$, this joining plane may or may not be a mirror plane for the two habit planes involved. For example, when plates I and II with habit planes (x –y 1) and ($-x$ –y 1), respectively, meet along a $(100)_{B2}$ plane, then the latter can be considered as a high symmetry plane. However, if for the same habit plane for plate I, plate II has a (x y 1) habit plane, this is no longer the case. Therefore, in total we can expect essentially four different configurations for this starting set of two crystallographically equivalent martensite plates, i.e., two per choice of macrotwin plane, one with the final interface being a mirror plane for the habit planes involved, the other one not. Changing the choice of the variant with the largest volume fraction does not affect this conclusion, although a permutation between the x and y co-ordinates is found for the habit plane normals. Another potentially relevant factor could be the common line between the habit planes of both plates. Indeed, when two plates meet they will first get in contact along this common line which could enforce a choice of actual macrotwin interface plane. In the first example used above, this common line belongs to the $(100)_{B2}$ plane, the high symmetry plane already considered. However, for the second example, i.e., when the habit plane choice for plate II changes, this common line belongs to the $(010)_{B2}$ plane.

At this point the small rotations of the microtwin planes with respect to their original $\{110\}_{B2}$ planes can be incorporated. The net angle of rotation θ can be calculated to be given by

$$\cos\theta = \frac{1 + \eta_3 z^2}{(1 + \eta_3)z}$$

with

$$z = \sqrt{\frac{\eta_1^{-2} + \eta_3^{-2}}{2}}.$$

with the rotation axis being $[-\kappa\chi, \chi, \kappa\delta]$. As both plates involved correspond to a different sign for κ and thus for the c-component of the rotation axis, this yields opposite rotation directions for both plates. Filling in typical values for the present austenite–martensite transformation it is found that a $(110)_{B2}$ family of microtwin planes with volume $\mathbf{U}_1$>volume $\mathbf{U}_2$ (i.e., plate I) yields a clockwise rotation of the intersection of the microtwin planes with the (x, y) plane (in the orientation of Fig. 3), whereas a $(1\text{–}10)_{B2}$ family with the same choice of variant ratio undergoes a counterclockwise rotation: these rotations are indicated in Fig. 3 as winged arrows. As a result, when two such plates meet along a $(100)_{B2}$ macrotwin plane an α angle>90° will be observed. Alternatively, when they meet along a $(010)_{B2}$ plane, this angle will be <90° as seen from the inset in Fig. 3.

The same conclusion can be reached in an intuitive manner when describing the martensitic transformation by its shearing mechanism depicted in Fig. 2b. Indeed, irrespective of the nucleation point and direction of growth of a plate with volume $\mathbf{U}_1$>volume $\mathbf{U}_2$ and microtwin planes parallel with $(110)_{B2}$ planes, the net shear of such a plate will, in order not to introduce too much strain, be compensated by a clockwise rotation (the arrows inside plate I in Fig. 3 indicate the shearing directions assuming a growth from left to right, cf. Fig. 2b), while the reverse is true for a plate with $(1\text{–}10)_{B2}$ microtwin planes. As a result, the net rotation of the lattice in $\mathbf{U}_1$ with respect to the original B2 lattice will be partially compensated and become smaller than that in $\mathbf{U}_2$.

The macrotwin boundaries described above, with close to perpendicular microtwin planes on either side, can thus be formed by using only two

out of the three available deformation variants. Because of the symmetry relations between the plates involved, some of these macrotwins are expected to lie along cubic planes of the austenite. If the third variant is allowed to participate in the microstructure, also macrotwin interfaces with an angle close to 120° between the two families of microtwins can be constructed, for example separating a $\mathbf{U}_1/\mathbf{U}_2$ plate from a $\mathbf{U}_2/\mathbf{U}_3$ plate. In the latter case, the macrotwin boundary is calculated to be along the $\{110\}_{B2}$ plane at ±60° from the $\{110\}_{B2}$ planes used for the microtwins on both sides [13]. As the 90° cases were most abundantly observed, only these cases will further be explored in the present paper.

We now observe that the compatibility conditions for two plates arising from different habit planes to be compatible across a macrotwin interface at zero-energy are exactly the same as for the existence of the wedge microstructure considered by Bhattacharya [13], with the macrotwin interface corresponding to the wedge midrib. Bhattacharya showed that for a cubic-to-tetragonal transformation it is impossible to have a zero-energy macrotwin with a $\{100\}_{B2}$ interface, and that the 120° case with a $\{110\}_{B2}$ interface can occur, but only if the deformation parameters satisfy the special relation

$$\eta_1^2 = \frac{(1-\eta_3^2)^2 + 4\eta_3^2(1+\eta_3^2)}{(1-\eta_3^2)^2 + 8\eta_3^4}$$

which is in fact very nearly satisfied in our case (using the present deformation parameters (see Section 6) the difference between both sides of the equation is 0.01407 or 1.6% of the absolute value, which falls within the total precision range calculated through propagation of this expression and based on a precision of 0.01 for the values of η_1 and η_3). This implies that the observed 90° configurations are expected to show structural features arising from the need to accommodate stresses that occur when both plates meet. As will be shown, some observations indeed point towards extra mechanisms for the relief of local stress.

In the above description, no attention was paid to the $L1_0$ type ordering of the lattice. This ordering becomes visible under HRTEM conditions when the corresponding projected structure reveals different atomic columns. This, combined with the need for edge-on microtwin planes to avoid overlapping effects, is the case only when looking along one of the shortened cubic directions of the austenite. The elongated direction then lies in the plane of the image. As a result, when observing a 90° macrotwin, the ordering in all variants can be made visible simultaneously with all microtwins being observed close to edge-on. The corresponding prior austenite direction is then [001] while the martensite variants are observed along <110] type directions. For the 120° macrotwins, the microtwins can only be observed edge-on when the viewing direction in the austenite is <111>. As a result, the martensite variants will be observed along <101] type directions and therefore no ordering will be visible in the variants.

5. Experimental observations

5.1. Mesoscale configuration of macrotwin boundaries

Experimentally, for both bulk and splat-cooled samples, a diversity of macrotwin boundaries is observed when viewed at a "mesoscale" (low and medium magnifications). Indeed, as illustrated in Fig. 4 the macrotwin boundaries can be almost a plane or they can reveal a zig-zag or wavy configuration. Still, even without descending to the atomic level, the fine structure of all these macrot-

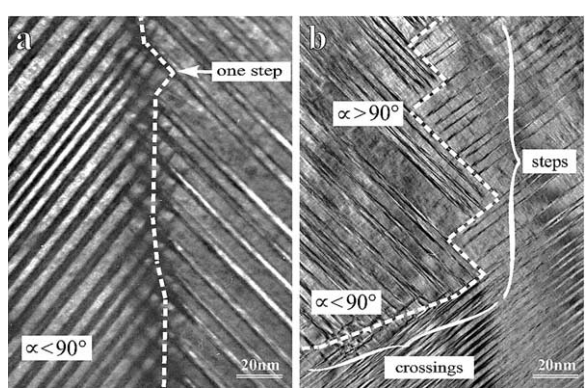

Fig. 4. Low magnification images of macrotwin boundaries revealing (a) crossing and (b) step type configurations.

win boundaries can be described using two basic constitutive elements. These two elements are clearly distinct and will be referred to as *crossing type* and *step type* elements. The crossings seen in Fig. 4a correspond to situations where the two plates have similar microtwin widths and the terminology refers to the fact that the deformations of one plate are seen to penetrate to some extent into the other plate. The resulting macrotwin boundary is a prior $\{100\}_{B2}$ plane. The steps in Fig. 4b reveal a configuration in which one set of microtwins ends at a twin plane of the other plate and this over a distance of several microtwins. This situation is seen to occur in cases where there is a strong but local variation in twin width on one or both sides of the interface. The single step in Fig. 4a is also found at a site where changes in the twin widths occur (finer on the left, broader on the right). Usually, the smallest twins seem to be stopped by the plate accommodating the widest twins, the latter thus providing the macrotwin interface which is, locally, a prior $\{110\}_{B2}$ plane.

The combination of these two constitutive elements can explain the diversity in macrotwin boundaries observed at a mesoscale. When the crossing type boundary is dominant, the interface is ideally a prior $\{100\}_{B2}$ plane as in Fig. 4a and in the lower part of Fig. 4b. When the step type boundary is dominant, a zig-zag configuration is observed which corresponds with the alternation of $(110)_{B2}$ and $(1\text{–}10)_{B2}$ planes for the interface as in the upper part of Fig. 4b. Note that a configuration with regular step sizes yields a macrotwin boundary with an average orientation again corresponding to a prior $\{100\}_{B2}$ plane. Finally, the combination of these two constitutive elements in a more or less random way and with differences in the width of the blocks can give wavy macrotwin boundaries or an abrupt change in the direction of the macrotwin boundary (bottom part of Fig. 4b), in which case the definition of an average direction for the macrotwin boundary is less relevant.

An alternative distinction on the mesoscale can be made by measuring the angle between the two families of microtwin planes. Irrespective of the step or crossing nature of the macrotwin interface, angles larger or smaller than 90° have been observed, as indicated in Fig. 4. The fact that even for a single macrotwin interface both cases can be measured, providing a drastic change in orientation of the boundary, as seen in Fig. 4b, indicates that this feature has some correlation with the plate growth, rather than with the original nucleation configuration. The comparison with 90° of course stems from the fact that the prior $\{110)_{B2}$ planes of these two sets of microtwin planes are perpendicular to one another. This angle will be referred to below as α.

In what follows we will focus on the crossing type boundaries, the details of the atomic structure around the step type boundaries being discussed in a previous publication [16].

5.2. Atomic structure at macrotwin boundaries

When observing the 90° macrotwin boundaries at high magnification and under atomic resolution conditions as in Fig. 5, it is seen that in every case the widest microtwin variants on both sides of the interface belong to the same deformation variant, e.g., $\mathbf{U}_1$ as in Fig. 3. Of course, as the corresponding variants and plates involved will be slightly rotated in different directions, the final orientation of the similar variants will also slightly differ. The angle γ defined above is measured as 12.5°, which yields a 6.25° rotation per variant when assuming the same but opposite rigid body rotation for each variant.

When boundaries with different angles between the two families of microtwin planes, i.e., larger or smaller then 90°, are compared on a HRTEM scale some systematic observations can be made, irrespective of the origin of the material. In Fig. 5 both cases are represented for crossing type boundaries from which it is seen that in the case where $\alpha < 90°$ the *c*-axis (Fig. 5a), i.e., the elongated direction, of the largest microtwin variant is close to parallel with the macrotwin interface. On the contrary, for $\alpha > 90°$ (Fig. 5b) this direction is close to perpendicular to this interface. Moreover, for the $\alpha < 90°$ case the tips of the smallest microtwin variants are seen to curve towards the macrotwin interface whereas for the $\alpha > 90°$ case they curve away from it, as indicated by arrows on the images. The actual measured angles between the two families of microtwin planes differ considerably from

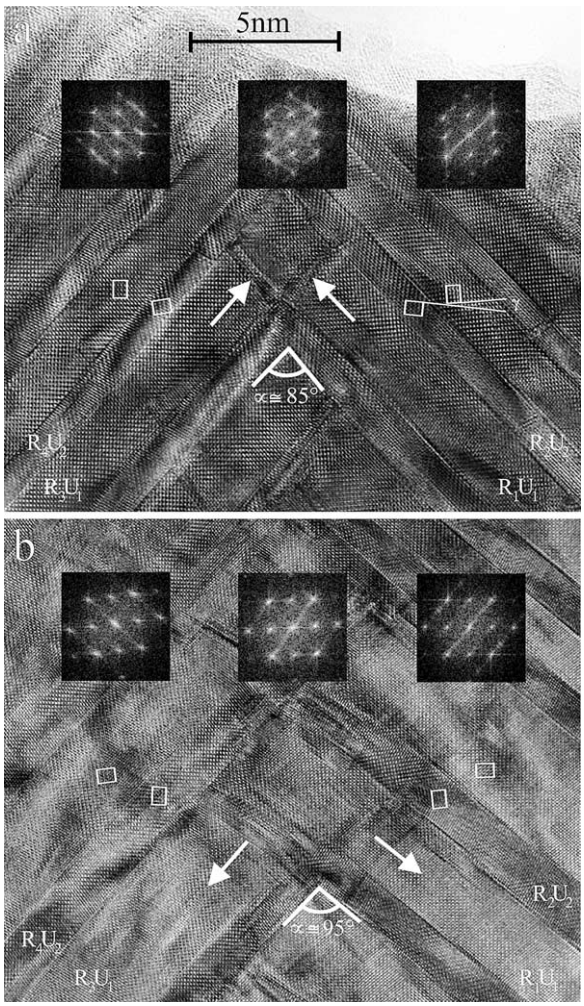

Fig. 5. $<110]$ martensite HRTEM images revealing the atomic configurations at crossing type macrotwin boundaries with (a) $\alpha < 90°$ and (b) $\alpha > 90°$. The rotation and deformation notations relate to those used in Fig. 3. The arrows indicate the direction of curvature for the small penetrating microtwin tips. The images corresponding to Fig. 5a and b are taken from bulk and splat-cooled material, respectively. The power spectra are incorporated in order to measure relative deformations and orientations.

interface to interface: values ranging from 84 to 97° have been found. Moreover, in some cases the microtwin planes are visibly bending or reorienting in areas between 50 and 500 nm away from the interface (see e.g. Fig. 6), in which case the above measurement depends on the actual choice of reference plane, i.e., close to or far away from the macrotwin.

On the HRTEM images in Fig. 5a and b, respectively from a bulk and a splat-cooled material, the general configuration of the crossing type boundary appears to be similar for both cases, irrespective of the difference in α. The two microtwin sequences are seen to penetrate each other so that all four twin variants are in contact and thus involved in the formation of the interface. This interface is not a sharp plane but rather a transition layer of approximately 5–10 nm wide around a prior $\{100\}_{B2}$ plane acting as a mirror and allowing for a gradual rotation of the atom planes from the core of one microtwin sequence into the other. This results in a mixed deformation region at the transition layer, as evidenced by the power spectra of the $\mathbf{U}_1$ variants in Fig. 5. To within an experimental error of 2%, all spectra show a rectangular pattern of the same size and x/y ratio, the only difference being their actual orientation. Thus, the atomic lattice in the central $\mathbf{U}_1$ region at the macrotwin interface has essentially the same lattice parameters as the lattice inside the plates, but it is rotated to an average orientation in between those on either side. As a continuous bending of a lattice implies local lattice deformations as well (compression below and elongation above), this indicates that most of the deformations needed to go from one plate to the other are accommodated in the tips of the small $\mathbf{U}_2$ variants separating the central $\mathbf{U}_1$ regions from those inside both plates. Indeed, these tips show a very blurred HRTEM image at the macrotwin interface, which can be attributed to severe local lattice deformations. The actual angle between the prior $[100]_{B2}$ directions in the $\mathbf{U}_1$ variants on either side of the interface is observed to be 6–8°, while that for the $\mathbf{U}_2$ variants is 14–16°, as measured from different areas and different plates. The observed difference between the large and small variants corresponds well with the fact that the rigid body rotation brings the larger variants closer to their undeformed orientation, as indicated in Section 4.

These central regions are further distinguished from the core of the plates by the small microtwin variants of one sequence penetrating into the broad variants of the other sequence. In these zones, the

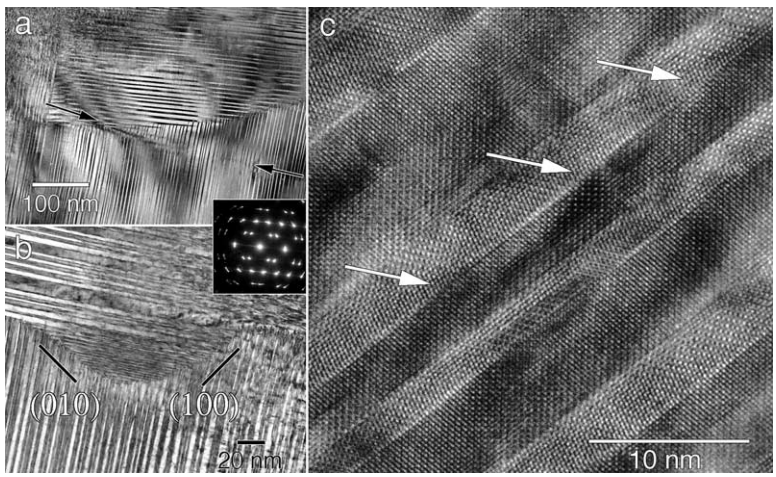

Fig. 6. Different examples of macrotwin interfaces incorporating extra deformations: (a) discontinuous reorientation of one family of microtwins at the sharp trace indicated by the arrow and (b) gradual bending of one family of microtwin planes, in two opposite directions depending on the macrotwin orientation, including an SAED pattern revealing lattice rotation by elongation of diffraction spots. Effects in (a) and (b) occur at relatively large distances from the macrotwin interface (50–500 nm). (c) HRTEM of atomic steps at the microtwin planes close to the macrotwin interface (10–50 nm).

penetrating microtwin variant tends to disappear with the formation of a needle usually tapered to the next microtwin boundary encountered in the penetrated laminate. These zones are subject to an extra bending deformation and occasionally to some tip splitting as observed in Fig. 5b.

As mentioned above, further away from the interface the microtwins are often seen to bend or reorient over a distance between 50 and 500 nm on either side, this distance being measured along the microtwin planes. This is clear from the overviews in Fig. 6a and b. In the first case, a discrete reorientation is observed at the trace in between the arrows, i.e., further and closer to the macrotwin interface the microtwin planes remain unrotated. In the second case, however, the microtwin planes are seen to bend gradually when approaching the macrotwin interface. This becomes evident when viewing the image at a grazing incidence along the nearly vertical microtwin traces. Moreover, this bending is in opposite directions in the left and right parts, i.e., at $(010)_{B2}$ and $(100)_{B2}$ type interfaces, respectively. This indicates that this accommodation feature is not only related to the relative orientations of both plates involved but also to the actual macrotwin plane. The observable curved elongations of the diffraction spots as seen in the selected area electron diffraction (SAED) pattern, obtained from a region with bending microtwins as in Fig. 6b, indicate that in such regions the martensite lattice is actually rotated over a few degrees along with the bending of the microtwins.

Closer to the macrotwin interface, i.e., within the 50 nm range again measured along the microtwin planes, HRTEM images as in Fig. 6c reveal a number of near-equidistant atomic scale ledges (arrows in Fig. 6c) shifting the microtwins over one atomic plane. At the same time, observing such lattice images along a grazing incidence parallel with the close packed planes shows that these planes are again slightly bent. This can only be confirmed by local power spectra in the few cases where good HRTEM images are obtained over a large area. Thus, in these areas at least, the bending is a combined result from microtwin ledges and lattice rotation. In some cases, presumably with large local stress accumulation, dislocations are also seen to add to the local deformations, although no direct correlation with the steps could be found.

The step type boundary locally involves two microtwin variants in a first plate but only one variant in the second plate and can thus be simplified to the case where one microtwin sequence meets a pure variant. The transition layer that will allow

the microtwin sequence to form a coherent interface with the pure variant is restricted to this microtwin sequence while the other sequence stays almost unaffected. The orientation difference due to the different rigid body rotations on both sides, is accommodated by a local lattice deformation within this single microtwinned plate. The deformation imposed is thus twice as large as the one required for each plate in the crossing type boundaries and can be explained in terms of a two-dimensional linear thermo-elasticity theory [16].

6. Discussion

The above presented images are only a small sample of the large number of different macrotwin interfaces that have been observed in the different $Ni_{65}Al_{35}$ samples. Still, the situation where a laminate with $\mathbf{U}_1$ broader than $\mathbf{U}_2$ meets a laminate with $\mathbf{U}_2$ broader than $\mathbf{U}_1$ was never observed so the focus will be on those interfaces with the same configuration of microtwin variants in the two plates involved. As in Fig. 3, in the following discussion the deformation variant $\mathbf{U}_1$ will be assigned to be the broader one and $\mathbf{U}_2$ the smaller one.

Macrotwin boundaries involving two deformation variants correspond to a situation where the angle α between the two families of microtwin planes is close to 90°, i.e., the angle between the prior {110} planes in the austenite. As such an interface involves contact regions between variants of the same type but with different rigid body rotations implied by their respective choice of microtwin orientation, it cannot be formed as part of an overall energy minimizing configuration including austenite–martensite interfaces surrounding the entire configuration [6,13]. By the same reasoning, if such plates are forced to make contact because of the nucleation and growth process, extra stress accommodating features are expected to be observed.

Alternatively, it can be shown [17] that if two plates with $(110)_{B2}$ and $(1\text{–}10)_{B2}$ microtwin planes and with the same relative volume fractions for the $\mathbf{U}_1$ and $\mathbf{U}_2$ variants are compatible over a macrotwin interface, then, assuming a zero-energy continuous deformation, the macrotwin plane must either be a former $(100)_{B2}$ plane or a former $(010)_{B2}$ plane. This is an important result as it provides a reason why $\{100\}_{B2}$ type interfaces are observed [6,13]. That this reasoning is not in contradiction with the previously mentioned non-existence of such an overall energy minimizing configuration, is due to the fact that now only compatibility over the central macrotwin is assumed and no surrounding austenite–martensite interfaces are taken into account. The angle between the microtwin planes for the $(100)_{B2}$ case is given by $90°+\gamma-\phi_1$, with

$$\tan\frac{\phi_1}{2} = \frac{\eta_3\rho}{\eta_1(1+\rho)}$$

and for the $(010)_{B2}$ case by $90°-\gamma+\phi_2$, with

$$\tan\frac{\phi_2}{2} = \frac{\eta_1\rho}{\eta_3(1-\rho)}$$

where

$$\rho = \lambda\frac{\eta_3^2-\eta_1^2}{\eta_3^2+\eta_1^2}.$$

Here it should be mentioned that the actual calculation leading to the present angles deals with rotating lattices which are directly translated into the reorientation of the microtwins involved. This is important to note as these calculated values will later on mostly be compared with measurements of the angles between traces of the microtwins as in Fig. 6b, rather than of lattice images as in Fig. 5. When ledges are involved, as in Fig. 6c, this relation cannot be retained completely as low magnification images will show curved microtwins with only minor lattice rotations. The difference between the values for the $(100)_{B2}$ versus $(010)_{B2}$ interface planes is due to the different orientations of the large (and small) variants with respect to these planes, which can be correlated with the observations of a perpendicular or parallel *c*-axis, respectively, of the large variant as described in Sections 4 and 5.2. In fact, these formulae are the continuum theory based analogues of the one obtained by Baele et al. for the $(010)_{B2}$ case in NiMn [18].

As already indicated in Section 4, some distinctions between different cases can be expected

based on simple geometric relations. Both cases suggested above, i.e., with the elongation direction of the broadest variant being parallel with or perpendicular to the macrotwin interface, were indeed observed for the crossing type boundaries. As long as the angle between the two families of microtwin planes is measured outside the stress accommodating region, it is reasonable to suppose that it is due to the original relative orientations of both plates, a feature definitely related with their nucleation and growth conditions. In other words, this angle is presumed to be a result of the original deviation of the microtwin planes in each plate from their prior $\{110\}_{B2}$ plane and should thus be compared with the calculation for θ. In practice, as the actual rotation axis is not exactly parallel with $[001]_{B2}$ (see Section 4), the calculated values for θ have to be transformed into the net angle α between the normals **n** of the macrotwin planes before being compared with the experimental measurements for α. Knowing the deformation parameters η_1 and η_3 this angle can thus be rigorously calculated as indicated in Section 4. As was also explained in Section 4, the rigid body rotation will bring the lattices of the largest variants closer to the situation of no rotation, e.g., the rectangle of variant $\mathbf{U}_1$ restores its vertical preference. Thus, contacting along the $(100)_{B2}$ plane produces an angle α larger than 90° whereas a $(010)_{B2}$ contact plane yields $\alpha < 90°$. At the same time, the $(100)_{B2}$ contact plane corresponds with a c-axis in U_1 being close to perpendicular to the macrotwin interface while the $(010)_{B2}$ macrotwin has this axis close to parallel with the interface. From the experimental images in Fig. 5 it is indeed seen that $\alpha > 90°$ (Fig. 5b) corresponds with the former while $\alpha < 90°$ (Fig. 5a) with the latter orientation of the $\mathbf{U}_1$ *c*-axis, confirming the conceptual discussion as well as the rigorous calculation.

When the measurements for the angles between both microtwin families are made at the interface, i.e., within the region accommodating extra deformations, the results should be compared with the calculations involving $\phi_{1,2}$. Still, as many different features at different length scales are seen to contribute to this accommodation, a straightforward comparison cannot be expected. Moreover, accurate calculations are difficult to perform as only the martensite lattice is observed in these samples. As a result, the deformation parameters η_1 and η_3 can only be obtained from martensite images such as Fig. 5 by assuming volume preservation, which is a typical characteristic of shape memory material and is indeed the case to within 1% for the present material. The validity of the measurement of the deformation parameters under the latter assumption, which yields $\eta_1 = 0.93$ and $\eta_3 = 1.15$, can be checked by comparing the calculated values for the angle γ and the volume fraction λ measured away from the macrotwin interface. In Table 1 a comparison between measured and calculated parameters is presented.

Comparing the calculated and observed values for γ and λ indicates that the assumption of volume preservation is indeed valid. As explained before, the observed value for α is measured between the microtwin orientations far away from the macrotwin interface while the calculated one originates from θ by taking the deviation of the rotation axis from $[001]_{B2}$ into account. Although the spread in measured values for α is relatively large, the expected order of magnitudes are in good agreement, and the directions of rotation are confirmed (as discussed above). From the respective numerical values for α and $90° \pm \gamma \mp \phi_{1,2}$ it is predicted that the stress accommodation close to the interface is expected to lead to a smaller deviation from the cubic 90° angle for the $\alpha > 90°$ case while it yields a larger deviation for the $\alpha < 90°$ case. However, the calculated differences between α and $\phi_{1,2}$ are relatively small, so that one can wonder whether this will have an observable effect. Still, as seen from the example in Fig. 6b where $\alpha =$ 92° for the $(100)_{B2}$ macrotwin and 88° for the $(010)_{B2}$ one, this angle is decreased for both macrotwin parts when approaching the interface. This is thus in good agreement with the predicted behaviour based on the continuum calculation for $\phi_{1,2}$. The large variation in measured values could possibly be related with the fact that local and possibly dynamic features that are not taken into account by the present model can play an important role in shaping the actual atomic and microstructural features of the macrotwin interfaces. Moreover, when measuring and comparing α and

Table 1
Calculated and measured microstructural parameters based on deformation parameters $\eta_1 = 0.93$ and $\eta_3 = 1.15$ measured in the assumption of volume preservation

	γ	λ	θ	$\alpha>90°$	$90°+\gamma-\phi_1$	$\alpha<90°$	$90°-\gamma+\phi_2$
Calculated	12.2°	0.35	2.9°	93.8°	92.4°	86.2°	85.2°
Observed	12.5°	0.35	–	92–97°	90–95°	83–86°	83–85°

$90° \pm \gamma \mp \phi_{1,2}$, it is assumed that the rotation of the lattice can be measured through the bending of the microtwins, which is overestimating the effect of $\phi_{1,2}$ as ledges are also observed to play a role in the microtwin bending (see Fig. 6c). Aside from these stress accommodation features away from and close to the interface, the highly strained tips of the smaller $\mathbf{U}_2$ variants as well as the averaged orientation of the $\mathbf{U}_1$ parts exactly at the macrotwin interface will also accommodate remaining stresses.

The difference in bending of the small variant tips as observed in Fig. 5 can possibly be explained by referring to the shear directions depicted in Figs. 2 and 3. As for the $\alpha > 90°$ case the shearing of the $\mathbf{U}_1$ variants is away from the interface it can be understood that this shearing also pulls the fine needles away from the interface when both transformation fronts cross. On the other hand, for the $\alpha < 90°$ case, the $\mathbf{U}_1$ shearing is directed towards the interface thus pushing the needles in the same direction. Both cases perfectly match the observations of Fig. 5, which could imply that these static observations reveal information on the actual growth directions of the plates. The fact that a single interface can change from $\alpha < 90°$ to $\alpha > 90°$ case, as in Fig. 4b, does not conflict with the above distinction. Indeed, suppose an interface is formed by growth of a small plate of type I into the side of a larger plate of type II (e.g., extend plate II to the left in Fig. 3 and let plate I touch it at its upper-right habit plane) the upper-left contact will produce an $\alpha < 90°$ macrotwin while the lower-right contact will yield an $\alpha > 90°$ case.

The above discussion is solely based on the observations of the crossing type boundaries. Of course, as also the step type boundaries consist of two plates with close to perpendicular microtwin planes, the growth and coalescence reasoning for the origin of the interfaces still holds. Moreover, in the nanometric scale a single interface often changes from crossing to step type. Overall, interfaces in splat-cooled material seem to accommodate more steps while in bulk material the preference is for crossings [19]. Recent TEM results on material obtained by melt-spinning, another rapid quench technique, also reveal a large number of step configurations at the macrotwin interfaces [20]. The only structural difference which could be detected from the still images of the final situations is the appearance of strong differences in local variant widths at the site of the steps. A detailed study of the local deformations at such steps using a combination of quantified HRTEM images and linear elasticity theory indicates that in these less symmetric cases the system takes advantage of the fact that large contact regions between two variants of the same deformation type can be avoided [16], which is indeed prohibited in the schemes of the elastic theories [6]. In a more general way, this difference could possibly reflect a competition between the elastic and surface energy contributions [21]. In order to avoid such contact regions, needles of the smallest variant are formed in one plate, ending at a flat edge of the same variant in the other plate. The choice for needle formation of the smallest variant is understandable as this implies less bending of the microtwin planes involved. This immediately dictates the type of variant which will form the actual interface as being of the same type. This way the primary contact regions are between $\mathbf{U}_1$ of the needle forming plate and $\mathbf{U}_2$ of the other plate, a contact which according to theory, can indeed provide energy minimisation [6]. For the latter, however, well defined orientation relations should appear which can indeed exist within a given plate but are violated by some degrees when dealing with variants

belonging to different plates. In order to compensate for this disadvantage the system includes an extra deformation in the plate containing the needles [16]. How to combine a nanoscale analysis of the stepped interfaces and the bending and tapering of needles with the present conclusions on mesoscopically flat macrotwins is still unclear. The correlation between the steps and deviations in local microtwin volume fraction indicates that the starting premises of the present theoretical approach are not fully met, probably due to additional local stress fields in the rapidly quenched materials. Any theory describing both flat and stepped interfaces in detail would need to include the latter.

There remains the question why only configurations with the same deformation variant for the widest twin bands are observed. Again, no definite answer to this question could be found from the final still images. Still, as the actual environment of a single grain or a set of growing martensite plates within a grain is most probably not perfectly isotropic, it could be argued that each austenite grain or each group of plates will (trans)form with a preferential direction for elongation. This would then single out one martensite variant to have a larger fraction within a given region of the sample which would imply a higher chance of observing a macrotwin with the same deformation variants for the widest twins on both sides. Alternatively, it can be expected that the elastic energy to achieve compatibility for the case of two plates with opposite volume fractions (though still same variants) is higher then for that of two equal fractions, so that the former cases imply the formation of even more complex microstructures that are no longer recognised in the TEM images as macrotwin boundaries. This is justified in more detail in Ref. [22] where the formation of macrotwins with the same families of microtwins in each plate is also found to be less probable on account of the large rotation of the plates required to achieve compatibility.

7. Conclusions

In the present work atomic scale details of martensite plate interfaces, so-called macrotwin boundaries, in Ni–Al are described and discussed. Only configurations with two families of microtwin planes at angles close to 90° are retained. These are interpreted as being due to the coalescence of separately nucleated and grown martensite plates. Depending on the original orientation of the distinct plates and the kinetics of the growth, two different configurations are observed. These can be distinguished by the angle between the microtwin planes on either side of the macrotwin interface being larger or smaller than 90°.

Irrespective of this angle, two configurations are found differing in local micro- and atomic structure. In the first, the so-called crossing type, a transition region of approximately 5–10 nm between both coalesced plates is observed in which the different rigid body rotations of both plates are compensated in a quasi-continuous manner. Small microtwin variants from one plate form bending needles tapering towards the perpendicular microtwin interfaces in the other plate, thus producing the crossed view of this type. This case occurs when the microtwin volume fractions on both sides of the macrotwin interface are similar. In the step type, occurring when clear differences between the microtwin volume fractions on both sides are observed, only one plate forms bending needles, which usually do not penetrate into the next plate.

While the described macrotwin configurations hold for both bulk and splat-cooled materials, the only difference which could be made between these materials is the relative amount of step type versus crossing type configurations. While a statistical analysis based on HRTEM results is hazardous, the step type configurations appear to be more commonly observed in splat-cooled material, which is believed to be related to the rapid quench nature of this preparation technique.

The observed orientation and measured angles are compared with predictions from thermo-elastic continuum theory. A proper correspondence for the relative orientations and the order of magnitude of the angles is obtained. Different stress accommodating features including continuous as well as discontinuous bending of the microtwins are observed. The need for such features and their average effect on the relative orientations is pre-

dicted on theoretical grounds. The large variety in observed structural features and the relatively large spread of experimentally measured values indicates that local and dynamic features further distort the actual structures.

Acknowledgements

The authors would like to thank K. Bhattacharya and R.D. James for stimulating discussions and D. Holland-Moritz for the preparation of the splat-cooled material. This work was supported by the Training and Mobility Research programme of the EEC under the project FMRX-CT98-0229 (DG12-BDN) entitled “Phase Transitions in Crystalline Solids” and within the Belgian IUAP project P4/10 “Systems with Reduced Dimensionality”.

References

[1] Au YK, Wayman CM. Scripta Metall. 1972;6:1209.
[2] Chakravorty S, Wayman CM. Metall Trans A 1976;7:555.
[3] Krasevec V, Delavignette P, Amelinckx S. Mat. Res. Bull. 1967;2:775.
[4] Krasevec V. Phys. Stat. Sol. (a) 1975;30:241.
[5] Schryvers D, Tanner LE. Ultramicroscopy 1990;32:241.
[6] Ball JM, James RD. Arch. Rat. Mech. Anal. 1987;100:13.
[7] James RD, Hane KF. Acta mater. 2000;48:197.
[8] Ball JM, James RD. Phil. Trans. Roy. Soc. London 1992;A338:389.
[9] Lieberman DS, Wechsler MS, Read TA. J. Appl. Phys. 1955;26:457.
[10] Bowles JS, Mackenzie JK. Acta metall. 1954;2:129.
[11] Bowles JS, Mackenzie JK. Acta metall. 1954;2:224.
[12] Khatchaturyan AG. Theory of structural transformations in solids. New York, USA: John Wiley & Sons, 1983.
[13] Bhattacharya K. Acta metall. mater. 1991;39:2431.
[14] Bhattacharya K. Arch. Rat. Mech. Anal. 1992;120:201.
[15] Bradley AJ, Taylor A. Proc. Roy. Soc. Lon. A 1937;159:56.
[16] Boullay P, Schryvers D, Kohn R. Phys. Rev. B 2001;64:144105.
[17] Ball JM, Schryvers D. In:Proceedings of the IUTAM Symposium on Mechanics of Martensite Phase Transformation in Solids. Sun QP, editor, Hong Kong: Kluwer, 2002, 27–36.
[18] Baele I, Van Tendeloo G, Amelinckx S. Acta metall. 1987;35:401.
[19] Schryvers D, Holland-Moritz D. Intermetallics 1998;5:427.
[20] Potapov PL, Ochin P, Pons J, Schryvers D. Acta mater. 2000;48:3833.
[21] Conti S. Private communication, 2000
[22] Ball J, Schryvers D. In: ICOMAT’02, Helsinki; 2002.